Fully differential single-photon double photoionization of atomic magnesium

F. L. Yip,[1] T. N. Rescigno,[2] and C. W. McCurdy[2,3]
[1]*Department of Science and Mathematics, California State University-Maritime Academy, Vallejo, California 94590, USA*
[2]*Chemical Sciences Division, Lawrence Berkeley National Laboratory, Berkeley, California 94720, USA*
[3]*Department of Chemistry, University of California, Davis, California 95616, USA*
(Received 14 October 2016; published 14 December 2016)

The valence-shell double ionization of atomic magnesium is calculated using a grid-based representation of the $3s^2$ electron configuration in the presence of a fully occupied frozen-core configuration of the remaining ten electrons. Atomic orbitals are constructed from an underlying finite-element discrete variable representation that facilitates accurate representation of the interaction between the inner-shell electrons with those entering the continuum. Length and velocity gauge results are compared with recent theoretical calculations and experimental measurements for the total double-, single-, and triple-differential cross sections, particularly at the photon energy of 55.49 eV for the last one. Comparison between the similar processes of double ionization of the ns^2 atoms helium, beryllium, and magnesium further illuminates the role of valence-shell electron correlation in atomic targets with heliumlike electronic configurations and symmetry.

DOI: 10.1103/PhysRevA.94.063414

I. INTRODUCTION

The process of double photoionization (DPI) from an atom or molecule remains one of the most sensitive probes of electron correlation and has been studied for many years to investigate the consequences of electron correlation in simple targets. The mechanism of removing two electrons via a single photoabsorption necessarily requires a correlated target, and the resulting angular distributions and possible energy sharing of the outgoing electrons from the Coulomb breakup problem requires an accurate nonperturbative treatment for theory and coincidence measurements of the fragments for experiment.

The prototypical system to study atomic double photoionization is helium and good agreement between experiment and theoretical formulations has led to an almost complete understanding of the double-photoionization dynamics in this simplest system [1,2]. Recent work has sought to advance double-ionization investigations by examining heliumlike systems, with several theoretical calculations approximating atomic targets that have ns^2 heliumlike configurations for removal by one photon. The alkaline-earth metals represent such systems for comparison, and numerous theories have been dedicated to studying these quasi-two-electron targets due to the large energetic and spatial separation between the core electrons and those in the valence shell that are removed by photoabsorption [3–12]. By extending these investigations to other targets that parallel the single-photon transition of DPI from helium in the initial and final states [13], the nature of the electron correlation between the outgoing electrons has been further elucidated as to consequences of the initially bound target orbitals [14,15] and the relative strength of the correlation energy compared to the nuclear attraction of the residual fragment left behind when two electrons are photoejected [16].

Most recently, theory and experiment have examined DPI from the valence shell of atomic magnesium, which has a neonlike core interacting with the $3s^2$ outer electrons. Experimental measurements [17,18] of the triple-differential cross section (TDCS), which measures the angular distributions of both electrons and their energy sharing above the double-ionization threshold have been recently compared to theoretical calculations using the convergent close coupling (CCC) [18] and time-dependent close coupling (TDCC) [19] methods at a photon energy of 55.49 eV. This energy is resonant with the state resulting from promotion of a $2p \rightarrow 3d$ electron embedded in the double continuum. A formulation that can fully take into account the dynamics of this resonant process currently lies beyond any theoretical treatment for examination of quasi-two-electron targets. Nevertheless, there have been comparisons of the experimental results undertaken with theoretical descriptions at this photon energy approximated by nonresonant *ab initio* calculations that feature only two active electrons [18,19] or by a semiempirical accounting of the Fano profile of the resonant transition [18].

The apparent agreement between experiment at the energy of the Mg($2p^6\,3s^2 \rightarrow 2p^5\,3s^2\,3d$) resonance and the previous theoretical studies that took no account of the resonance stimulated us to examine the TDCS for double photoionization of magnesium using exterior complex scaling (ECS) to examine the three-body Coulomb breakup dynamics at this energy and compare with other theoretical calculations at 55.49 eV and for the total double-ionization process in this atom, for which other experimental measurements exist [20].

The formalism we employ to study this process requires denoting the neonlike core occupancy of all but the valence electrons, which provide a closed-shell Coulomb and exchange interaction with the outer $3s^2$ electrons that feel the action of the photon toward the double continuum. The construction of atomic orbitals out of an underlying radial grid to represent these core electrons facilitates the approximation of holding them fixed in a configuration-interaction expansion and has been applied to atomic beryllium in both a time-independent formalism for one-photon double ionization [8,9,13] and in a time-dependent framework [11,21] for consideration of two-photon processes that remove the outer electrons. This method has also been applied to examine the double-photoionization process for neon [22], which unlike the systems considered here, leaves behind an open-shell target with distinct final-state couplings for the residual dication. For the second-column

ns^2 targets, however, only a single final-state channel remains because the resulting ionic fragment has a neonlike core configuration.

Section II overviews the description of the magnesium target in a combined orbital-grid basis for resolution of the double-photoionization amplitudes that describe the fully differential cross sections in photoionization. Results are presented in Sec. III and compared with experimental measurements and theoretical calculations, with particular focus on the double-ionization process at 55.49 eV. We also examine the similarities between helium, beryllium, and magnesium in the angular distributions of double ionization at 20 eV excess photon energy to highlight the nature of the photoionization process. Concluding remarks are presented in Sec. IV in which we offer an explanation for why the resonant excitation that enhances the cross section and facilitated the experimental measurements of DPI at 55.49 eV seems to have little effect on the angular distribution of the ejected electrons.

II. THEORETICAL FRAMEWORK

The methods utilized in this work for treating photoionization of two electrons from a target with additional electrons has been previously described in greater detail both in a time-independent framework [8,9] and with a time-dependent treatment involving ultrashort laser pulses [11,21]. Thus, here we provide a brief overview of the most important points in applying the method to magnesium. Atomic units are used throughout the following, unless otherwise stated.

The two-active-electron approximation to magnesium relies on a frozen-core approximation for the remaining ten electrons. The wave function can be expanded in configurations with $N-2$ core electrons held fixed in atomic orbitals throughout. Within this frozen-core approximation, the problem then can be regarded as an effective two-electron problem involving a full configuration interaction (CI) of the $3s^2$ valence electrons of magnesium in the presence of the $1s^2\,2s^2\,2p^6$ core, the full Hamiltonian being

$$H = h(1) + h(2) + \frac{1}{r_{12}}, \tag{1}$$

where the correlation between the valence electrons to be ejected by the photoabsorption is represented by $1/r_{12}$ and the interaction of the remaining electrons on the valence shell is represented by the one-body operator h,

$$h = T - \frac{Z}{r} + \sum_{\text{occ}} [2J_{\text{occ}} - K_{\text{occ}}], \tag{2}$$

where T is the one-electron kinetic energy, $-Z/r$ with $Z = 12$ represents the attraction of the magnesium nucleus, and the terms in the sum over occupied orbitals, $2J_{\text{occ}}$ and K_{occ}, account for the direct and exchange interaction felt by the $3s^3$ valence electrons of the fully occupied core orbitals. Specifically, the direct operator for the nl closed-shell orbital is given by

$$J_{nl}(\mathbf{r}) = \int \frac{|\varphi_{nl}(\mathbf{r}')|^2}{|\mathbf{r}-\mathbf{r}'|} d\mathbf{r}', \tag{3}$$

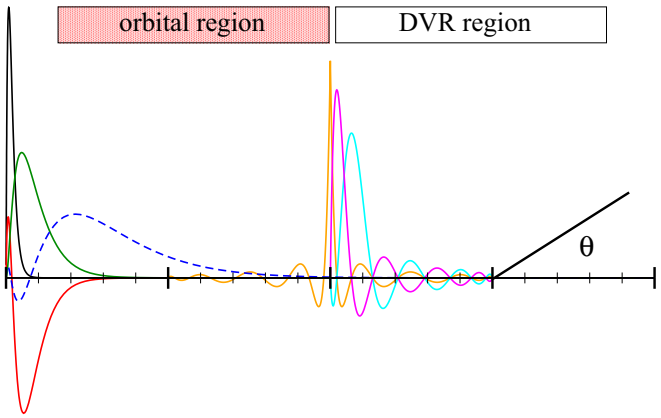

FIG. 1. Radial space in an orbital-DVR basis representation. Over the orbital region where the occupied $1s$, $2s$, and $2p$ frozen-core orbitals of Mg (shown as solid lines on the left) from the first M underlying FEM-DVR basis functions are transformed into orthogonal orbitals (e.g, the $3s$ of neutral Mg, shown as the dashed line) via the unitary transformation in Eq. (5). Representation of the radial coordinate by the underlying primitive FEM-DVR basis functions (solid lines at the center of the figure) proceeds beyond the range of the orbitals. The overall radial basis is orthonormal in this scheme. ECS of the coordinate in the outer DVR region is also facilitated with no complications to the orbital transformation.

while the nonlocal-exchange component as defined according to its operation on the orbital $\chi(\mathbf{r})$ is

$$K_{nl}(\mathbf{r})\chi(\mathbf{r}) = \varphi_{nl}(\mathbf{r}) \int \frac{\varphi^*_{nl}(\mathbf{r}')\chi(\mathbf{r}')}{|\mathbf{r}-\mathbf{r}'|} d\mathbf{r}'. \tag{4}$$

The nl closed-shell orbitals that provide the Coulombic screening and nonlocal exchange are taken here to be the $1s$, $2s$, and $2p$ Hartree-Fock orbitals of neutral magnesium. They are plotted as solid lines on the left half of the schematic shown in Fig. 1. The double-ionization potential of the valence shell for the target Mg atom is given by the ground-state energy of the valence-electron Hamiltonian in Eq. (1), with the energy of the neonlike fixed-core common to both the bound and continuum states.

To construct these operators and describe the bound, single-, and double-continuum representation on a radial grid, we have employed an adaptation of the finite-element method with discrete variable representation (FEM-DVR) [23] that uses atomic orbitals as the basis in a subset of the finite elements. We summarize the basic idea here, and significantly more detail is provided in Refs. [8,11]. The transformation of an ordinary finite-element DVR [23] suitable for describing the radial coordinates of a simple atomic target (e.g., helium) to account for core electrons is referenced to the occupied orbitals of the multielectron atom. Over a suitably defined orbital region where the orbitals describing the core electrons are significantly nonzero, the first few finite-element regions are transformed to form an orthogonal complement to the radial orbitals of the core electrons. The transformation from a primitive FEM-DVR basis $\chi_j(r)$ with M functions spanning the orbital region to an orthogonal set of atomic orbitals is

represented by

$$\varphi_\alpha(r) = \sum_{j=1}^{M} U_{\alpha j}\chi_j(r), \tag{5}$$

where within the orbital region the atomic orbitals $\varphi_\alpha(r)$ built from the underlying FEM-DVR functions describe the coordinates of all electrons and facilitate the construction of appropriate atomic CI configurations with both active and frozen electrons upon which to expand the description of bound, single-, and double-continuum states of the target. An essential point is that the basis orbitals, $\varphi_\alpha(r)$, which are used to expand the wave function of the two active electrons, are orthogonal to the frozen occupied atomic orbitals of the atom.

Beyond the region of the atomic orbitals, the underlying FEM-DVR description is untransformed, providing a flexible grid-based representation of the electronic coordinates that has been used in a variety of applications involving continuum electron dynamics [24]. The regions of radial space partitioned in this manner are shown schematically in Fig. 1. The Hartree-Fock orbitals of the core electrons that provide a reference for the transformation operator $U_{\alpha j}$ in Eq. (5) over the entire orbital region are shown as solid lines, along with the $3s$ orbital of Mg, shown as a dashed line on the left of Fig. 1, which provides the first of the orthonormal atomic orbitals that can be populated in the expansion configurations. Figure 1 also highlights another key feature of this method in the large r untransformed FEM-DVR region: the use of exterior complex scaling on the radial coordinates far from the atomic orbitals,

$$r \to \begin{cases} r, & r \leqslant R_0, \\ R_0 + (r - R_0)e^{i\theta}, & r > R_0, \end{cases} \tag{6}$$

to properly handle the asymptotic behavior of the continuum electrons and solve the double-ionization problem on a relatively small radial grid (see Ref. [24] for a full treatment of the ECS).

Finally, in summarizing the orbital FEM-DVR process that has been previously applied to both closed-shell atoms and open-shell targets, we mention that it is precisely the most cumbersome part of an orbital transformation from an underlying primitive basis, the manipulation of the two-electron integrals, that is greatly facilitated by the diagonal representation of the underlying FEM-DVR basis. What is generally a four-index transformation to construct the correlating electronic repulsion $1/r_{12}$ in Eq. (1) is simplified to (at most) a two-index transformation,

$$\langle\varphi_\alpha\varphi_\beta|\varphi_\gamma\varphi_\delta\rangle = \sum_{i,j=1}^{M} U_{\alpha i}U_{\beta j}U_{\gamma i}U_{\delta j}f(i,j), \tag{7}$$

where $f(i,j)$ is a primitive FEM-DVR two-electron repulsion integral. This computational savings is a result of the diagonal nature of local potentials in the underlying FEM-DVR basis.

With the orbital-DVR radial basis, we describe the wave function for the two active electrons, initially bound as $3s^2$ valence electrons of magnesium, as

$$\Psi(\mathbf{r}_1,\mathbf{r}_2) = \sum_{l_1 l_2} \frac{1}{r_1 r_2}\psi_{l_1,l_2}(r_1,r_2)\mathcal{Y}^{LM}_{l_1,l_2}(\hat{\mathbf{r}}_1,\hat{\mathbf{r}}_2), \tag{8}$$

where $\mathcal{Y}^{LM}_{l_1,l_2}(\hat{\mathbf{r}}_1,\hat{\mathbf{r}}_2)$ is a coupled-spherical harmonic describing the angular degrees of freedom, and the atomic symmetry permits the decomposition into the partial-wave radial wave function $\psi_{l_1,l_2}(r_1,r_2)$.

The double-ionization amplitudes that describe the ionization processes ejecting two electrons into the continuum are given by solving a driven Schrödinger equation

$$(E - H)\Psi^{+}_{\rm sc}(\mathbf{r}_1,\mathbf{r}_2) = (\boldsymbol{\epsilon}\cdot\boldsymbol{\mu})\Psi_0(\mathbf{r}_1,\mathbf{r}_2), \tag{9}$$

where $E = E_0 + \omega$ is the total energy available to share by the electrons above the double-ionization potential E_0, ω is the photon energy, and the driving term on the right of Eq. (9) represents the action of the photon with linear polarization ϵ onto the $3s^2$ valence state of magnesium Ψ_0 in the dipole approximation, where $\boldsymbol{\mu}$ represents the dipole operator. The scattered wave solution $\Psi^{+}_{\rm sc}(\mathbf{r}_1,\mathbf{r}_2)$ determined by solving this equation on a grid with exterior complex scaling imposing the outgoing wave boundary conditions contains all continuum processes at energy E.

To isolate the double-continuum amplitudes for electrons with momenta $\mathbf{k}_1$ and $\mathbf{k}_2$,

$$f(\mathbf{k}_1,\mathbf{k}_2) = \sum_{l_1,l_2}\left(\frac{2}{\pi}\right) i^{-(l_1+l_2)}e^{i\eta_{l_1}(k_1)+i\eta_{l_2}(k_2)} \times \left[\mathcal{F}_{l_1,l_2}(k_1,k_2)\mathcal{Y}^{LM}_{l_1,l_2}(\hat{\mathbf{k}}_1,\hat{\mathbf{k}}_2)\right], \tag{10}$$

from the single-ionization channels, we employ a surface integral formulation for the partial wave amplitudes by integrating along a surface using testing functions that are continuum states of the individual one-body Hamiltonian h of the residual dication as defined in Eq. (2). Further details of this implementation can be found in Refs. [8,9,24]. Here we provide the final result for these partial amplitudes,

$$\mathcal{F}_{l_1,l_2}(k_1,k_2) = \frac{\rho_0}{2}\int_0^{\pi/2}\left[\varphi^{k_1}_{l_1}(r_1)\varphi^{k_2}_{l_2}(r_2)\frac{\partial}{\partial\rho}\psi_{l_1,l_2}(r_1,r_2) - \psi_{l_1,l_2}(r_1,r_2)\frac{\partial}{\partial\rho}\varphi^{k_1}_{l_1}(r_1)\varphi^{k_2}_{l_2}(r_2)\right]\Big|_{\rho=\rho_0} d\alpha. \tag{11}$$

The triply differential cross sections, representing the most detailed information that can be known in the double-ionization process, can be computed from the double-ionization amplitudes as

$$\frac{d^3\sigma}{dE_1 d\Omega_1 d\Omega_2} = \frac{4\pi^2\omega}{c}k_1k_2|f(\mathbf{k}_1,\mathbf{k}_2)|^2, \tag{12}$$

in the length gauge. Integrating over all angles Ω_1 and Ω_2 of both electrons yields the single-differential cross section (SDCS), which exhibits the energy sharing of the outgoing electrons for the total continuum energy. Integration of the SDCS over the possible energy sharing yields the total double-ionization cross section at the photon energy ω,

$$\sigma = \int_0^E \frac{d\sigma}{dE_1}dE_1. \tag{13}$$

Having defined these cross sections and provided a brief overview of the time-independent treatment, we present in

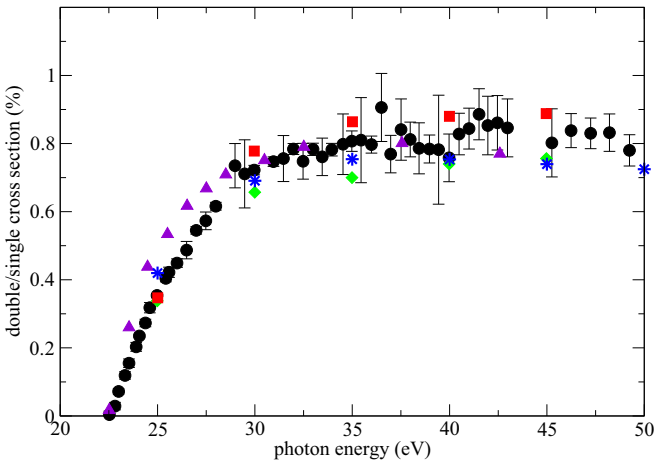

FIG. 2. Double- to single-ionization cross-section ratios for single-photon double ionization of Mg. Blue stars: present results in the length gauge; red squares: TDCC results [10]; green diamonds: RMPS results [10]; violet triangles: CCC results [14]; black circles: experimental measurements [20].

the next section the results of valence-shell double ionization of magnesium.

III. RESULTS

The wave function of the ground state ^1S state of magnesium is determined by diagonalizing the Hamiltonian in Eq. (1), constructed on a purely real radial grid with an extent $r = 32.0$ bohrs. The orbital region range is determined by the extent of the core $1s$, $2s$, and $2p$ orbitals and was taken to consist of three finite elements with 16th-order DVR in each,

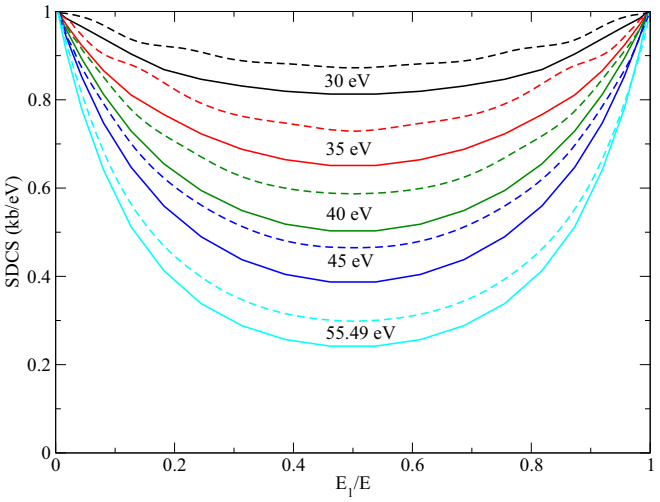

FIG. 3. Energy differential cross sections for DPI of magnesium for different photon energies. Results have been normalized to unity. Solid lines: present results calculated in the length gauge. The scaling factors to recover the absolute SDCS are (in kb/eV) 0.218 for 30 eV, 0.147 for 35 eV, 0.108 for 40 eV, 0.086 for 45 eV, and 0.057 for 55.49 eV. Dashed lines: TDCC calculation results [19], with scaling factors (in kb/eV) of 0.238, 0.173, 0.133, 0.106, and 0.073 for this list of photon energies, respectively. 1 kb $= 10^{-21}$ cm^2.

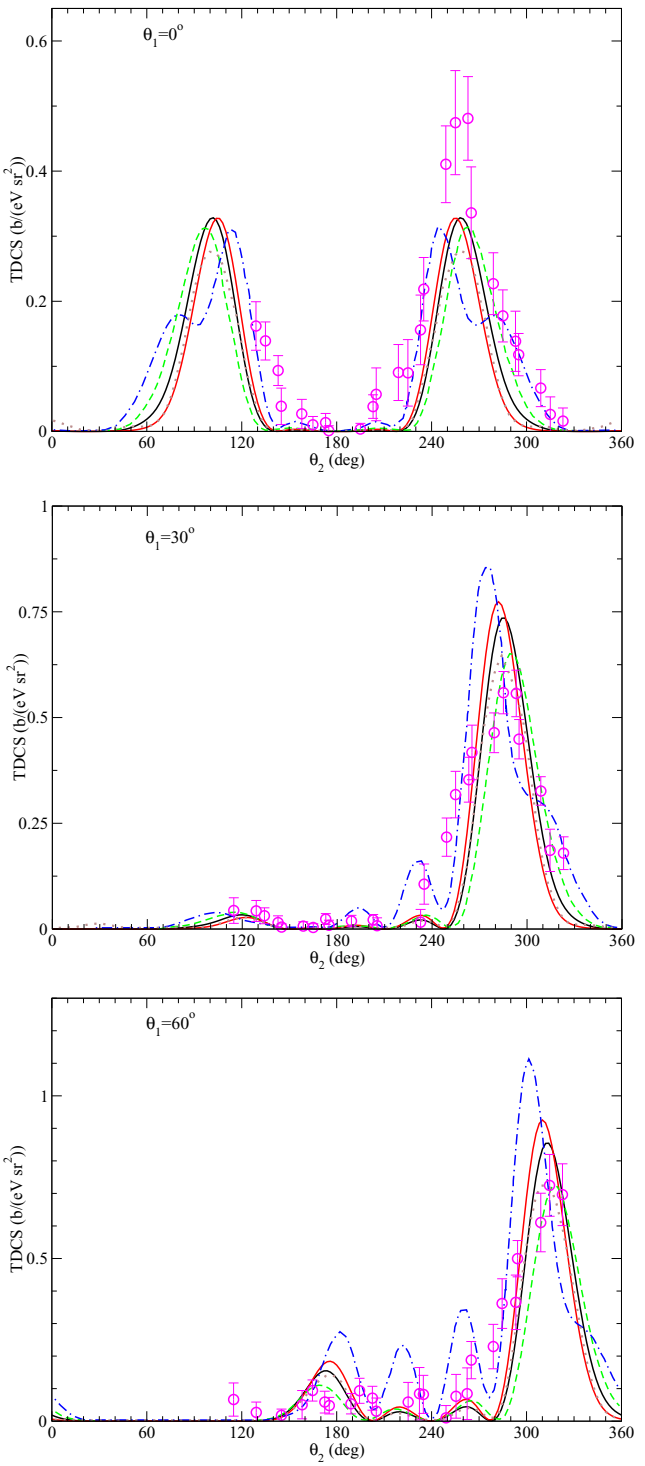

FIG. 4. TDCSs for DPI from magnesium at 55.49 eV photon energy for equal energy sharing. Each panel shows plots the second electron in the coplanar geometry when the first electron is fixed at the angle shown relative to the polarization. Solid (black) curve: present results in the length gauge; solid (red) curve: present results in the velocity gauge; dashed (green) curve: TDCC results [19]; dotted (brown) curve: CCC nonresonant results; dashed-dot (blue) curve: CCC resonant results [18]; magenta circles: experimental measurements [18]. 1 b $= 10^{-24}$ cm^2.

with endpoints of 0.5, 8.0, and 16.0 bohrs. The maximum electron angular momentum used to converge the TDCS results below was found to be $l_{max} = 9$. With these grid parameters, the double-ionization potential of the $3s^2$ shell of magnesium is 22.8 eV, in excellent agreement with the experimentally determined value of 22.7 eV [25] and with other theoretical treatments [19].

The solution of the driven equation (9) proceeds on a larger grid with 8.0 bohr finite elements up to an ECS radius at $R_0 = 72.0$ bohrs with two additional complex-scaled finite elements (ECS angle $\theta = 30^o$) to impose the outgoing wave boundary conditions. TDCS results for the photon energies considered were observed to be converged with respect to the grid parameters, maximum individual electron angular momenta l_{max}, and amplitude extraction radius.

A. Double- to single-ionization cross-section ratios

In Fig. 2, we present the calculated ratio of the total double-ionization cross section to the single-ionization cross section. These results are calculated in the length gauge and compared with theoretical results from compared convergent close coupling (CCC) [14], time-dependent close coupling (TDCC) [10], and the *R*-matrix-with-pseudostates (RMPS) [10] and with experimental measurements of Wehlitz *et al.* [20]. We note that velocity gauge results (not shown) agree within a few percent with the presented length gauge results. The agreement of the double- to single-ionization ratios is good with the other theoretical treatments and tracks very well with the experimental measurements. All points of this ECS calculation lie within the experimental error bars at the photon energies presently considered.

B. Single-differential cross sections

The energy-sharing cross section (SDCS) is shown in Fig. 3 for length gauge results at different photon energies and normalized to unity to plot them in a common panel. The absolute cross-section scaling factors for each photon energy are noted in the caption. The profile of these single-differential cross sections, peaking at the unequal energy-sharing extremes with a minimum at equal energy sharing $E_1 = E_2$ is typical of double ionization from ns^2 heliumlike atoms. The theoretical results of TDCC [19] are also shown for comparison as dashed lines, exhibiting a similar evolution of the SDCS towards more extreme energy sharing as the photon energy is increased. The magnitude of the these cross sections is lower than the TDCC results, as seen in the total double- to single-ionization ratios plotted in Fig. 2. The agreement between these calculations in magnitude and qualitative behavior is good, with differences most likely resulting from the description of the interaction of the active electrons with the core.

C. Triple-differential cross sections at $\omega = 55.49$ eV

The most sensitive probe of electron correlation that can be revealed in a double-ionization investigation is contained in

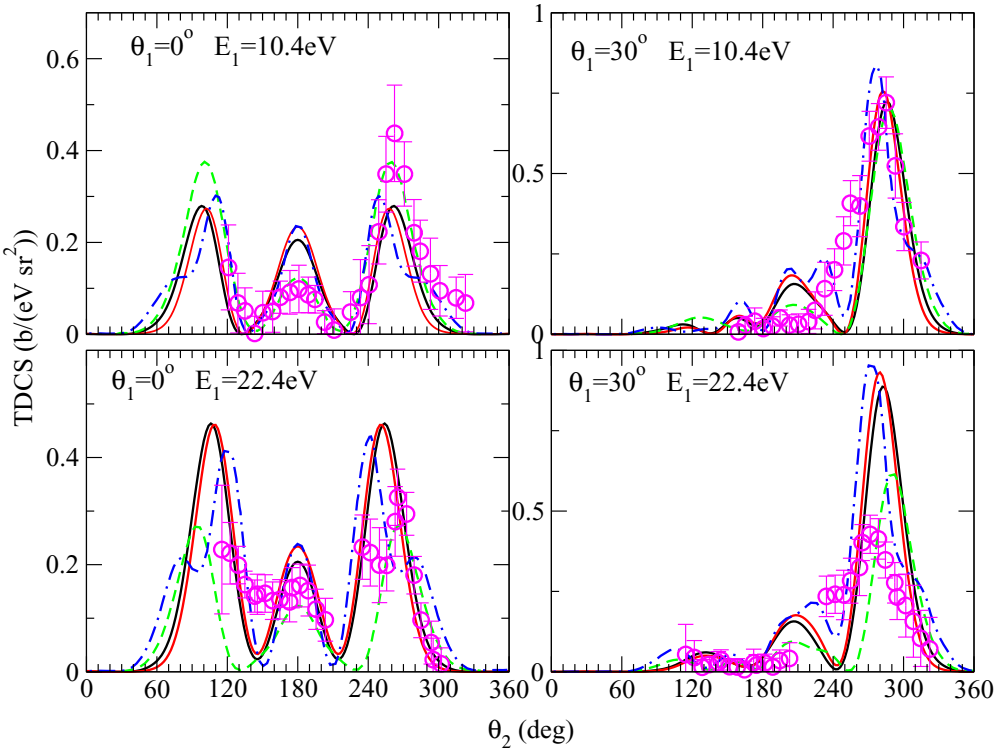

FIG. 5. TDCSs for DPI from magnesium at 55.49 eV photon energy for unequal energy sharing at two different fixed electron directions: $\theta_1 = 0^\circ$ (left panels) and $\theta_1 = 30^\circ$ (right panels) relative to the polarization. The fixed-direction electron has 10.4 eV and 22.4 eV in the upper and lower rows, respectively. Solid (black) curve: present results in the length gauge; solid (red) curve: present results in the velocity gauge; dashed (green) curve: TDCC results [19]; dashed-dot (blue) curve: CCC resonant results [18]; magenta circles: experimental measurements [18]. 1 b = 10^{-24} cm^2.

the triple-differential cross section, which exhibits the angular distributions of both exiting electrons and their energy sharing. For these heliumlike cases absorbing a single photon, the overall transition features a symmetry of $^1S \rightarrow {}^1P$. The main features due to electron correlation are most constrained by symmetry at equal energy sharing. Figure 4 shows the TDCSs plotted in the coplanar geometry (with both electrons exiting in the plane of the polarization, which defines the z axis for the angular measurements, i.e., $\phi_1 = \phi_2 = 0^\circ$) at a photon energy of $\omega = 55.49$ eV. Each panel plots the cross section as a function of the angle of the second electron when the other electron (labeled electron 1) is held fixed at the angle indicated.

The results shown for both length and velocity gauges exhibit a known parity symmetry that requires the TDCS to be zero for back-to-back electron ejection when $E_1 = E_2$ for heliumlike targets [26]. The TDCS plotted for the present results are absolute, with good agreement seen between the different gauges, indicating a suitably converged description of the initial target state valence electrons within the frozen-core approximation. Experimental measurement points measured at Elettra [18] are also shown in each panel, as are the results from previous theoretical calculations: the TDCC results [19] and CCC calculations [18]. Following the comparison and discussion in Refs. [18,19], the nonresonant CCC calculation results are absolute while the resonant CCC calculation (employing a semiempirical treatment to account for the resonance process populating the $3d$ state of the target) has been scaled by a factor of $3q^2$, where q is the Fano q parameter, taken here with a value of 50 [18]. The TDCC results are also absolute. We note that, additionally, all of the results for comparison have been divided by a factor of 2 from the figures in Ref. [19] due to an alternative definition of the TDCS (see Ref. [8]).

The experimental results, gathered in the same measurement, are internormalized between the panels and can be compared after consistent scaling (here taken to be a factor of 0.011 which was the scaling chosen in Ref. [19]). The present results show fairly good agreement with the absolute theoretical treatments in the number of lobes and the relative sizes of the secondary peaks compared to the primary peaks. Slight differences in the predicted angles of these peaks are apparent, but the equal-energy-sharing results are consistent with the symmetry conditions for the heliumlike double photoionization at equal energy sharing. All theories seem to produce a smaller result than the experiment at $\theta_1 = 0^\circ$, producing better agreement of the size of the dominant peak with the experimental measurements at $\theta_1 = 30^\circ$ and $\theta_1 = 60^\circ$. At these angles in particular, the present results are slightly larger than the absolute TDCC and CCC (nonresonant) calculations. The secondary features along the primary lobes predicted by the semiempirical CCC calculation that incorporates the resonant nature of the transition at this photon energy are not found in the *ab initio* two-active-electron theories and are not particularly well resolved in the experimental points. We note that all the theoretical results show narrower dominant peaks than observed for helium double photoionization at 20 eV above threshold, consistent with the spatially more diffuse initial state orbital of the magnesium target [15].

In Fig. 5, the length and velocity gauge TDCS results for unequal energy sharing at $\omega = 55.49$ eV are shown in the coplanar geometry for fixed directions $\theta_1 = 0^\circ$ and $\theta_1 = 30^\circ$ and two different unequal-energy-sharing cases, representing the fixed electron at these angles carrying 31.7% of the excess energy in the top row, and the complementary E_1 carrying 68.3% of the available energy (32.8 eV) in the lower row. The relaxation of the parity selection rule away from equal energy sharing is evident in these figures compared to Fig. 4. We find good agreement in the overall shape of the TDCS lobes with different theories, being most in accord for the upper-right panel.

In Fig. 6, we report the length and velocity gauge TDCS results for both equal energy sharing and the unequal energy sharing of Fig. 5 with the first electron direction fixed at $\theta_1 = 90^\circ$. No experimental measurements were reported at the fixed electron direction perpendicular to the polarization $\theta_1 = 90^\circ$, but we compare with the theoretical descriptions. All theories show a pair of dominant and secondary lobes symmetric about $\theta_2 = 270^\circ$. The resonant CCC results show significantly larger secondary peaks for both equal and unequal energy sharing, while all nonresonant calculations predict smaller values for the secondary lobes compared to the primary

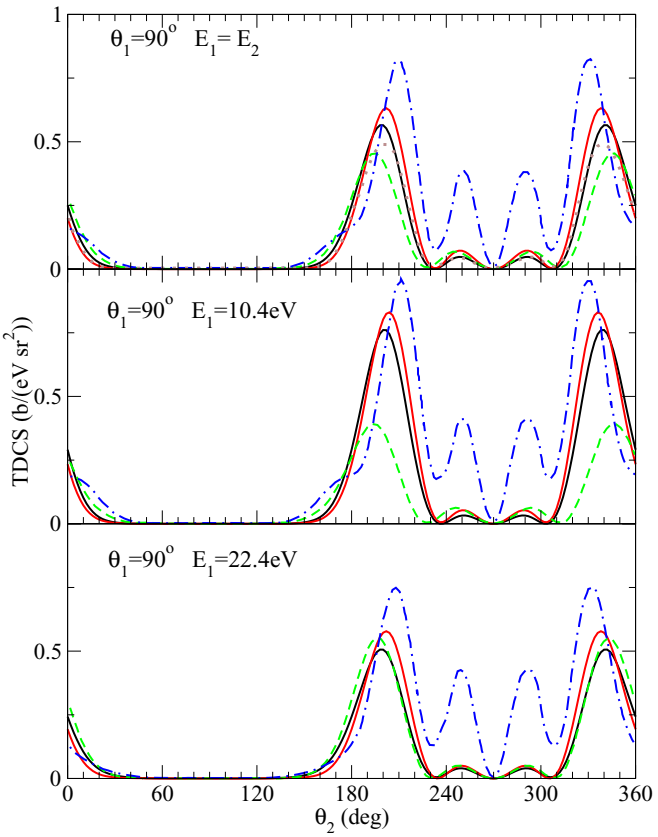

FIG. 6. TDCSs for DPI from magnesium at 55.49 eV photon energy for various energy sharing with fixed electron direction $\theta_1 = 90^\circ$ relative to the polarization. From top to bottom, the fixed-direction electron has 16.4, 10.4, and 22.4 eV. Solid (black) curve: present results in the length gauge; solid (red) curve: present results in the velocity gauge; dashed (green) curve: TDCC results [19]; dashed-dot (blue) curve: CCC resonant results [18]. 1 b = 10^{-24} cm^2.

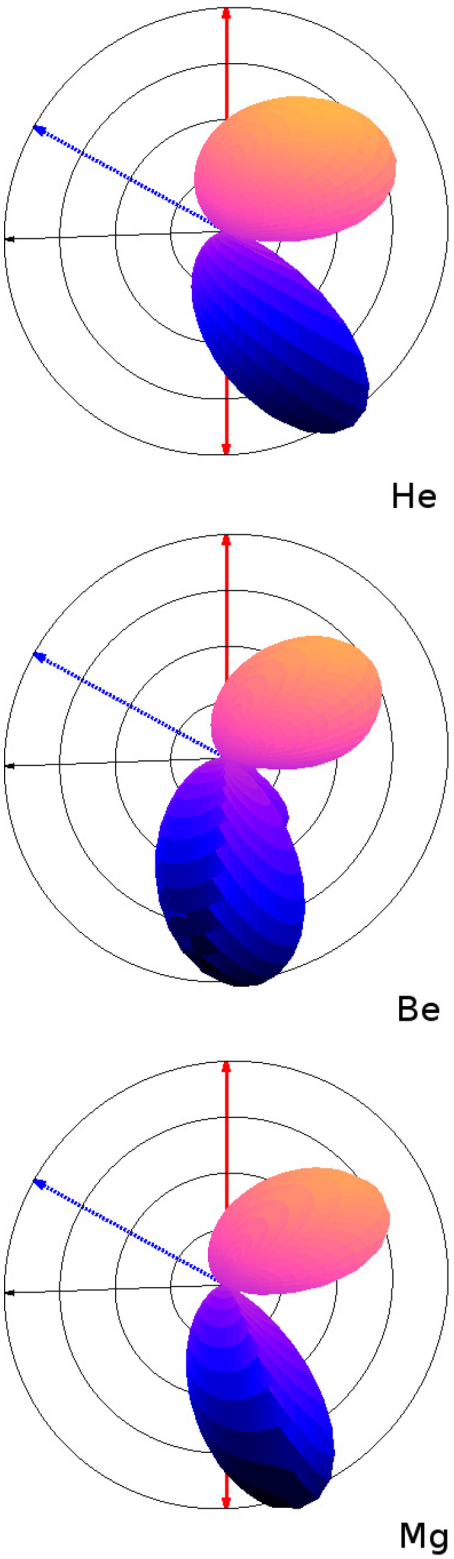

FIG. 7. Normalized angular distributions for valence-shell photoionization of He, Be, and Mg at 20 eV excess photon energy. The fixed-direction electron at $\theta_1 = 60^\circ$, represented by the dotted blue arrow from the polarization (solid red arrows), carries 5% of the excess energy.

peaks. The location of the primary peaks differs slightly between the different theoretical results, with the largest variation between the present results and the other calculated results most prominent when the fixed electron is slow (middle panel). We also note less variation in the magnitude of these cross sections as a function of the fixed electron rotating away from the polarization direction than is seen for helium.

Finally, to compare the different ns^2 atomic targets that have been treated by the present method, we present in Fig. 7 the normalized angular distribution of the second electron plotted outside the plane of the polarization and fixed electron for 5% energy sharing of 20 eV excess energy above the double-ionization potential for helium, beryllium, and magnesium. The fixed electron is at $\theta_1 = 60^\circ$ in each panel. Comparing these results shows a similar lobe structure in each, with slight variation in the width of the primary and secondary lobes as the initial state of the target becomes more diffuse. There is noticeable variation in the angle of the lobes across these different targets when compared at the same excess photon energies, but the general structure of the TDCS is similar. The indication of these comparisons and with those of the previous theoretical and experimental results is that the symmetry of the one-photon process in these overall $^1S \rightarrow {}^1P$ transitions determines many of the features of the TDCS, with variations in the angles and relative sizes of the lobes of photoejection distribution slightly sensitive to the details of the correlated initial state.

IV. DISCUSSION

We have presented single-photon double-ionization cross sections for removal of the valence electrons of atomic magnesium. As a function of photon energy, good agreement between the total double- to single-photoionization cross sections exists between the present results and other theoretical calculations and experiment. We also find good agreement with the energy-sharing cross-section profiles at different photon energies with the TDCC treatment.

Focusing on the results at the photon energy of 55.49 eV for which experimental TDCS results have been collected via a resonant process, we find fairly good agreement with other *ab initio* theoretical results that similarly cannot account for the resonant transition of the experimental conditions. Nevertheless, comparison of the experimental measurements with the various theoretical calculations reveals common structures in the general shape of the triple-differential cross sections for several angles and energy sharing. The most substantial impact of the resonant transition for the experiment that is unaccounted for in the *ab initio* calculations affects the absolute magnitude of the cross sections at the relative sizes of the secondary lobes compared to the dominant photoejection angles for the cases considered. Overall, reasonable agreement is found between the experimental angular distributions and the various theoretical treatments, which is significantly determined by the overall symmetry of the heliumlike $^1S \rightarrow {}^1P$ single-photon transition.

It is only natural to question why the measured TDCS shows little effect of the $2p \rightarrow 3d$ resonance state despite the fact that the photon energy is centered on that transition. Indeed, the semiempirical resonance model used in Ref. [18] does little to

improve agreement and introduces structures in the TDCS not evident in the experiment. Energy considerations dictate that the $(2p^5\,3s^2\,3d)$, ^1P state can only decay into the $(2p^6\,kl\,k'l')$, ^1P double continuum, as well as a number of single-continuum channels, with $(2p^6\,3s\,kp)$, ^1P being the most likely. The simplest description of decay into the latter channel involves a single two-electron matrix element, $\langle 3s\,3d||2p\,kp\rangle$, while decay of the resonance state into the double continuum is a thee-electron transition and reduces to a consideration of the two matrix-element products $\langle 3d|kd\rangle\,\langle 3s^2||2pkp\rangle$ and $\langle 3s|ks\rangle\,\langle 3skp||2pkp\rangle$. Unlike the case of direct double photoionization, DPI via the resonant transition only involves the $(kpkd)$ and $(kskp)$, ^1P double continua. We would therefore expect a significant impact on the TDCS if this decay route were important. But we note that the presence of the $\langle 3d|kd\rangle$ and $\langle 3s|ks\rangle$ bound-free overlap integrals, which are quite small, evidently minimizes the influence of this decay channel on the TDCS. We conclude that the resonance state decays predominantly into the single continuum and thus has little effect on the measured TDCS, which explains the success of the two-active-electron treatments.

ACKNOWLEDGMENTS

Work performed at California State University, Maritime, was supported by the National Science Foundation, Grant No. PHY-1509971. Work performed at Lawrence Berkeley National Laboratory was supported by the US Department of Energy, Office of Basic Energy Sciences, Division of Chemical Sciences, Contract No. DE-AC02-05CH1123. Work at the University of California, Davis, was supported by the US Department of Energy Grant No. DE-SC0007182. We made use of the resources of the National Energy Research Scientific Computing Center, a DOE Office of Science User Facility supported under Contract No. DE-AC02-05CH11231.

[1] L. Avaldi and A. Huetz, J. Phys. B **38**, S861 (2005).
[2] L. Malegat, Phys. Scr. **2004**, 83 (2004).
[3] A. S. Kheifets and I. Bray, Phys. Rev. A **65**, 012710 (2001).
[4] J. Colgan and M. S. Pindzola, Phys. Rev. A **65**, 022709 (2002).
[5] F. Citrini, L. Malegat, P. Selles, and A. K. Kazansky, Phys. Rev. A **67**, 042709 (2003).
[6] D. C. Griffin, M. S. Pindzola, C. P. Ballance, and J. Colgan, Phys. Rev. A **79**, 023413 (2009).
[7] S. Laulan and H. Bachau, Phys. Rev. A **69**, 033408 (2004).
[8] F. L. Yip, C. W. McCurdy, and T. N. Rescigno, Phys. Rev. A **81**, 053407 (2010).
[9] F. L. Yip, F. Martín, C. W. McCurdy, and T. N. Rescigno, Phys. Rev. A **84**, 053417 (2011).
[10] M. S. Pindzola, C. P. Ballance, S. A. Abdel-Naby, F. Robicheaux, G. S. J. Armstrong, and J. Colgan, J. Phys. B **46**, 035201 (2013).
[11] F. Yip, A. Palacios, T. Rescigno, C. McCurdy, and F. Martín, Chem. Phys. **414**, 112 (2013).
[12] M. W. McIntyre, A. J. Kinnen, and M. P. Scott, Phys. Rev. A **88**, 053413 (2013).
[13] F. L. Yip, C. W. McCurdy, and T. N. Rescigno, Phys. Rev. A **81**, 063419 (2010).
[14] A. S. Kheifets and I. Bray, Phys. Rev. A **75**, 042703 (2007).
[15] A. S. Kheifets, I. Bray, J. Colgan, and M. S. Pindzola, J. Phys. B **44**, 011002 (2011).
[16] F. L. Yip, D. A. Horner, C. W. McCurdy, and T. N. Rescigno, Phys. Rev. A **75**, 042715 (2007).
[17] E. Sokell, P. Bolognesi, A. Kheifets, I. Bray, S. Safgren, and L. Avaldi, Phys. Rev. Lett. **110**, 083001 (2013).
[18] E. Sokell, P. Bolognesi, A. Kheifets, I. Bray, S. Safgren, and L. Avaldi, Phys. Rev. A **89**, 013413 (2014).
[19] S. A. Abdel-Naby, M. S. Pindzola, and J. Colgan, J. Phys. B **48**, 025204 (2015).
[20] R. Wehlitz, P. N. Juranić, and D. V. Lukić, Phys. Rev. A **78**, 033428 (2008).
[21] F. L. Yip, A. Palacios, F. Martín, T. N. Rescigno, and C. W. McCurdy, Phys. Rev. A **92**, 053404 (2015).
[22] F. L. Yip, T. N. Rescigno, C. W. McCurdy, and F. Martín, Phys. Rev. Lett. **110**, 173001 (2013).
[23] T. N. Rescigno and C. W. McCurdy, Phys. Rev. A **62**, 032706 (2000).
[24] C. W. McCurdy, M. Baertschy, and T. N. Rescigno, J. Phys. B **37**, R137 (2004).
[25] Yu. Ralchenko, A. E. Kramida, J. Reader, and NIST ASD Team, NIST Atomic Spectra Database (Ver. 4.1.0), 2012.
[26] F. Maulbetsch and J. S. Briggs, J. Phys. B **28**, 551 (1995).